Structure and Stability of Ago2 MID-Nucleotide Complexes: All-in-One (Drop) His_6-SUMO Tag Removal, Nucleotide Binding, and Crystal Growth

Li Lei,[1] Joel M. Harp,[1] John C. Chaput,[2] Kelly Wassarman,[3] Mark K. Schlegel,[3] Muthiah Manoharan,[3] and Martin Egli[1,4]

[1]Department of Biochemistry, School of Medicine, Vanderbilt University, Nashville, Tennessee
[2]Department of Pharmaceutical Sciences, University of California, Irvine, California
[3]Alnylam Pharmaceuticals, Cambridge, Massachusetts
[4]Corresponding author: *martin.egli@vanderbilt.edu*

Published in the Nucleic Acid Chemistry section

The middle (MID) domain of eukaryotic Argonaute (Ago) proteins and archaeal and bacterial homologues mediates the interaction with the 5′-terminal nucleotide of miRNA and siRNA guide strands. The MID domain of human Ago2 (hAgo2) is comprised of 139 amino acids with a molecular weight of 15.56 kDa. MID adopts a Rossman-like beta1-alpha1-beta2-alpha2-beta3-alpha3-beta4-alpha4 fold with a nucleotide specificity loop between beta3 and alpha3. Multiple crystal structures of nucleotides bound to hAgo2 MID have been reported, whereby complexes were obtained by soaking ligands into crystals of MID domain alone. This protocol describes a simplified one-step approach to grow well-diffracting crystals of hAgo2 MID-nucleotide complexes by mixing purified His_6-SUMO-MID fusion protein, Ulp1 protease, and excess nucleotide in the presence of buffer and precipitant. The crystal structures of MID complexes with UMP, UTP and 2′-3′ linked α-L-threofuranosyl thymidine-3′-triphosphate (tTP) are presented. This article also describes fluorescence-based assays to measure dissociation constants (K_d) of MID-nucleotide interactions for nucleoside 5′-monophosphates and nucleoside 3′,5′-bisphosphates. © 2024 The Authors. Current Protocols published by Wiley Periodicals LLC.

Basic Protocol 1: Crystallization of Ago2 MID-nucleotide complexes
Basic Protocol 2: Measurement of dissociation constant K_d between Ago2 MID and nucleotides

Keywords: Ago2 • crystal structure • equilibrium constant • protein-nucleic acid interaction • RNA

How to cite this article:
Lei, L., Harp, J. M., Chaput, J. C., Wassarman, K., Schlegel, M. K., Manoharan, M., & Egli, M. (2024). Structure and stability of Ago2 MID-nucleotide complexes: All-in-one (drop) His_6-SUMO tag removal, nucleotide binding, and crystal growth. *Current Protocols*, *4,* e1088. doi: 10.1002/cpz1.1088

CURRENT PROTOCOLS
A Wiley Brand

Current Protocols e1088, Volume 4
Published in Wiley Online Library (wileyonlinelibrary.com).
doi: 10.1002/cpz1.1088

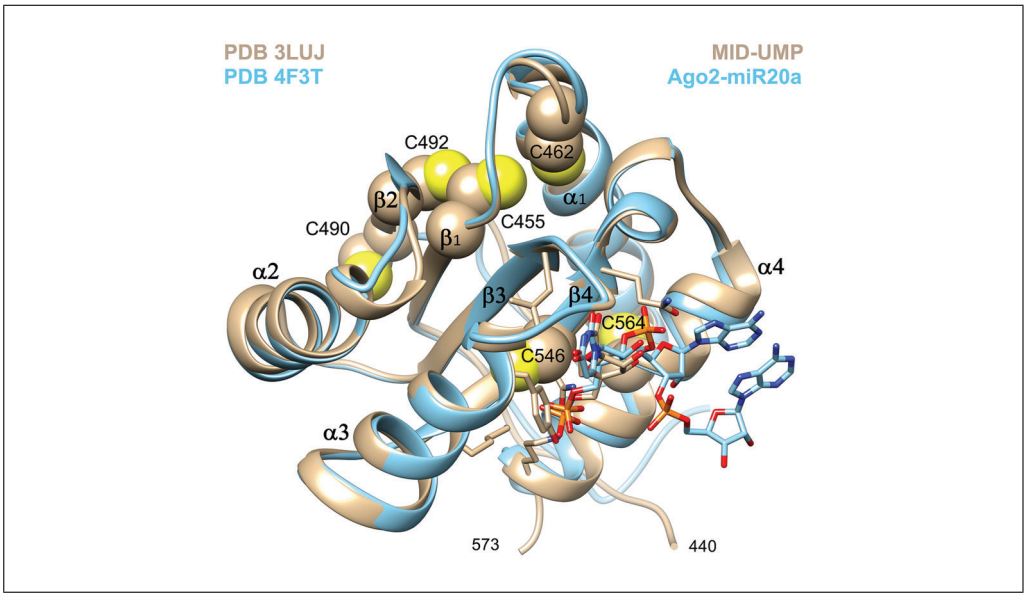

Figure 1 Overlay of the MID domains from crystal structures of the domain alone in complex with UMP (Frank et al., 2010), PDB ID 3LUJ *www.rcsb.org* (Berman et al., 2000), and full-length Ago2 in complex with miR-20a (Elkayam et al., 2012), PDB ID 4F3T. The root mean square deviation (r.m.s.d.) for 982 atom pairs is 1.36 Å. Secondary structure elements of the Rossmanoid fold are labeled, and cysteines are highlighted in space filling mode. The nucleotide specificity loop between β3 and α3 and adjacent to the uracil base is visible in the center of the image. Only the first three nucleotides of the miRNA bound to Ago2 are shown. Illustration generated with the program UCSF Chimera (Pettersen et al., 2004).

INTRODUCTION

The human Ago2 MID domain is a compact protein of 139 amino acids in length (N439 to L578) that forms the binding site for the 5′-terminal nucleotide of miRNA and siRNA guide strands. Other important Ago2 domains are PIWI that harbors the endonuclease for cleaving the target strand and PAZ that binds to the 3′-terminal dinucleotide overhang of the siRNA guide (Elkayam et al., 2012; Schirle & MacRae, 2012). MID adopts an alpha-beta sandwich fold and contains six cysteines that do not engage in disulfide bridges in crystal structures of full-length Ago2 and MID alone (Fig. 1).

The MID domain forms a relatively shallow depression that harbors the binding site for the 5′-terminal phosphate of the guide strand residue (AS1, Fig. 2). The electrostatic surface potential (ESP) inside and around the depression is strongly positive, thereby promoting not just binding of 5′-monophosphorylated species but also ATP (Fig. 2A). Viewed from the side, the ribose 2′- and 3′-oxygen atoms and a portion of the six-membered ring of adenine are visible, consistent with the shallow nature of the binding pocket that only buries the 5′-phosphate (Fig. 2B). An overlay of the MID domain complex and the structure of the complex between full-length Ago2 and miR-20a demonstrates that the second guide strand residue (AS2) is exposed and not buried inside the pocket (Fig. 2C).

The positive ESP of the MID binding pocket and the area around it also permit binding of m^7GpppG dinucleotide and trapping the complex in a crystal (Fig. 3). The 5′-phosphate of m^7G is located roughly at the site where the 5′-phosphate of NMPs and the α-phosphate of ATP are bound. However, the additional phosphates then curl around and emerge from the binding pocket such that there is no interaction between G and any MID side chains. The observation that both ATP and m^7GpppG produce complex crystals attests to the importance of the electrostatic contribution to the binding affinity. However, no structures of more standard di- or trinucleotides, e.g., 5′-pUpU or 5′-pUpUpU, respectively, bound to MID domain alone have been reported to date.

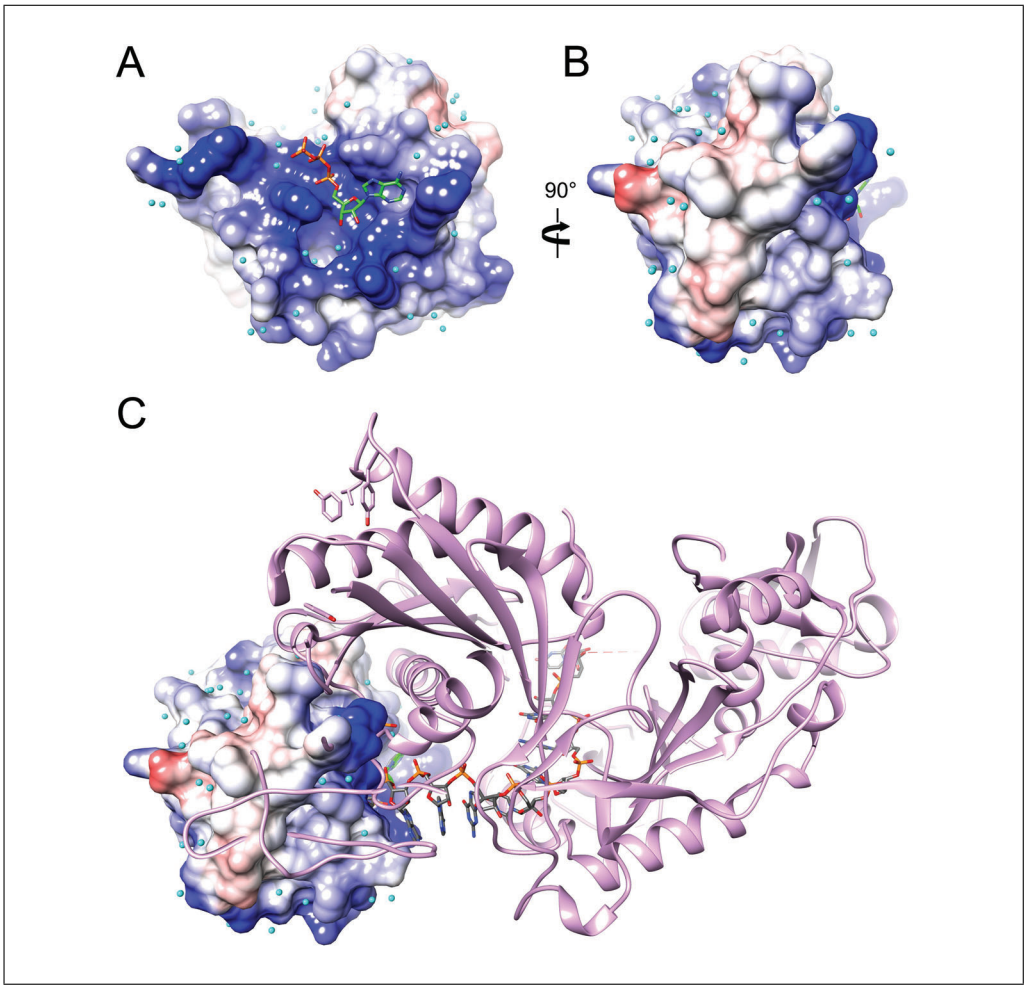

Figure 2 The complex between human Ago2 MID domain (residues 439-575) and ATP (Frank et al., 2011), PDB ID 3QX9. The complex viewed (**A**) into the binding pocket, and (**B**) rotated around the vertical by 90°. The surface of the domain is colored according to ESP, from blue (most positive) to red (most negative). Water molecules in the crystal structure of the MID domain complex are shown as small spheres colored in cyan. (**C**) Overlay between the MID domain complex and full-length Ago2 bound to miR-20a (Elkayam et al., 2012), PDB ID 4F3T. Ago2 is shown as a pink ribbon cartoon and miR-20a is shown with carbon atoms colored in gray. Illustrations generated with the program USCF Chimera (Pettersen et al., 2004).

Frank et al. (2010) reported crystal structures of MID complexes with UMP and AMP. MID crystals were grown from solutions containing 10 to 15 mg/ml protein that were mixed 1:1 with a solution containing 0.1 M imidazole (pH 8), 0.2 M NaCl, 0.46 M NaH_2PO_4, and 1.84 M K_2HPO_4. Native crystals were then soaked in a drop containing 0.2 M $(NH_4)_2SO_4$, 0.1 M Na cacodylate buffer (pH 6.5), 15% PEG 8000, 20% glycerol, and 20 mM NMP. However, unlike the complexes with UMP and AMP obtained in this fashion, the occupancy of CMP and GMP in the MID structures was insufficient to place these nucleotides into the binding pocket and refine the structures of the corresponding complexes (Frank et al., 2010). One reason for this limitation may be related to the soaking approach, i.e., CMP and GMP could not displace phosphate bound to MID in crystals that were grown in the presence of high concentrations of phosphate buffer. We also know from stability data that the MID complexes with UMP ($K_d = 0.12$ mM) or AMP ($K_d = 0.26$ mM) are more stable than those with CMP ($K_d = 3.6$ mM) or GMP ($K_d = 3.3$ mM) (Frank et al., 2010). Both uracil and adenine use their Watson-Crick edges to engage in H-bond interactions with residues from the P523 to P527 loop (G524 and T526, Fig. 4). In the complex with AMP, there is an additional interaction between Q548 and the N3 of adenine. By comparison, neither cytosine nor guanine can establish these

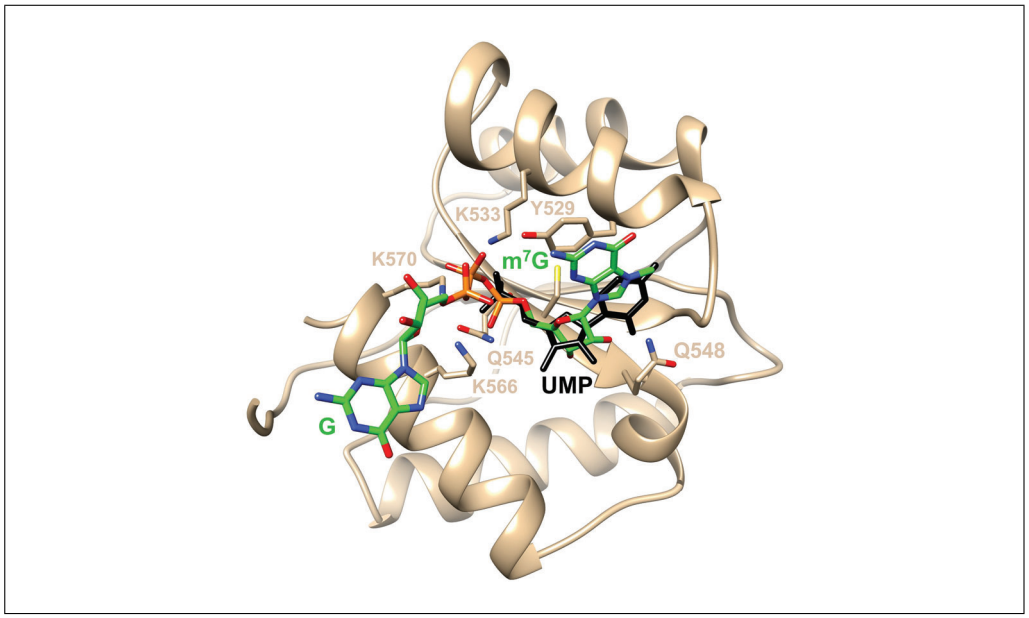

Figure 3 Crystal structure of the complex between Ago2 MID domain and m^7GpppG (Frank et al., 2011), PDB ID 3QX8. m^7GpppG carbon atoms are colored in green, UMP from the crystal structure of the complex with MID (Frank et al., 2010), PDB ID 3LUJ, is shown with solid bonds in black to indicate its position relative to m^7Gp and selected MID side chains are labeled. Illustration generated with the program UCSF Chimera (Pettersen et al., 2004).

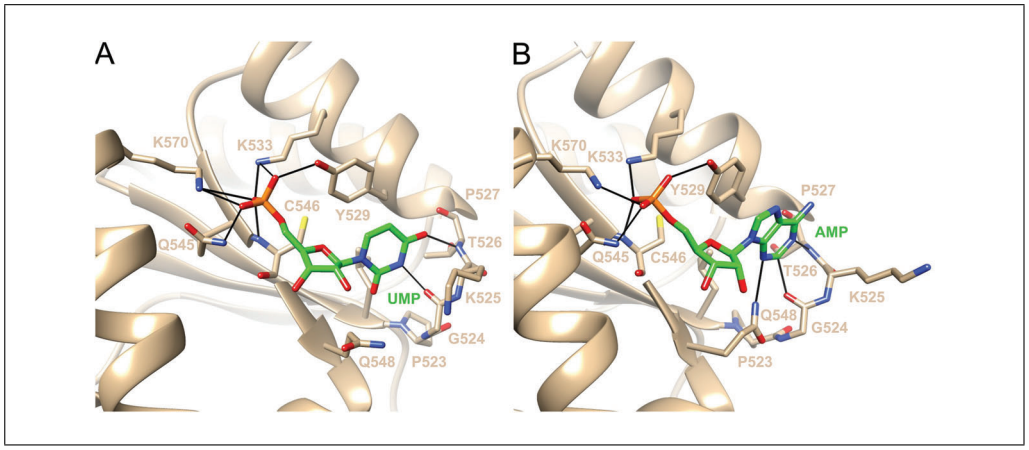

Figure 4 H-bond interactions between MID side and main chain atoms and (**A**) UMP, PDB ID 3LUJ, and (**B**) AMP, PDB ID 3LUD (Frank et al., 2010). Carbon atoms of nucleotides are highlighted in green, MID residues are labeled and H-bonds are drawn with thin solid lines. Illustrations generated with the program UCSF Chimera (Pettersen et al., 2004).

interactions; thus, structures of these 'complexes' deposited in the Protein Data Bank (PDB) just contain phosphate in the MID binding pocket. It is possible that GMP is in a conformational equilibrium and binds as a mixture of the nucleoside in the *syn* and *anti* conformations (see the *syn* conformation of m^7G in Fig. 3).

As pointed out above, the complex with m^7GpppG shows that dinucleotides can in principle be trapped in MID crystal structures. Moreover, comparison of MID in complex with UMP and full-length Ago2 in complex with miR-20a reveals that MID residues can potentially form stabilizing interactions not just with AS1 but also AS2: Q548, K550, and N551 with P2, and Q558 and N562 with the nucleobase (Fig. 5). However, the nucleoside portion of AS3 appears outside the reach of any MID side chain, although K566 can potentially interact with the second phosphodiester moiety (P3, Fig. 5). MID also

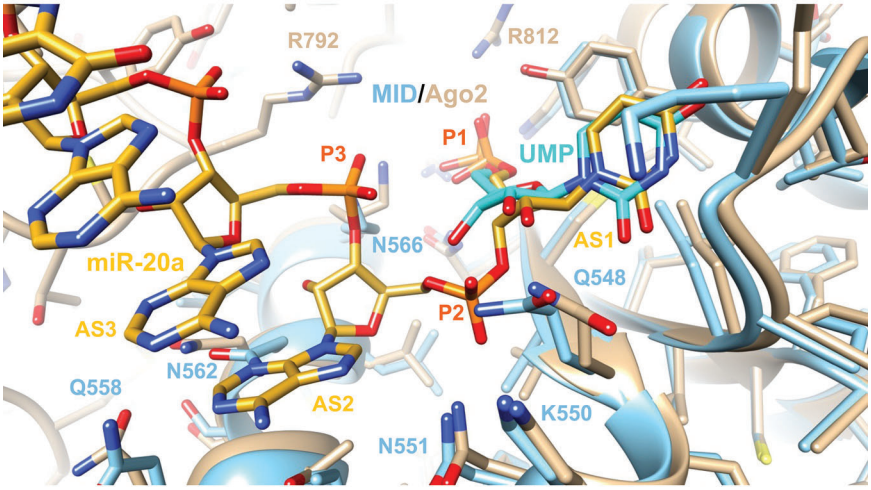

Figure 5 Overlay of the MID domain in complex with UMP, shown as light blue ribbon and with carbon atoms colored in cyan, respectively (Frank et al., 2010), PDB ID 3LUJ, and Ago2 bound to miR-20a, shown as a beige ribbon and with carbon atoms colored in goldenrod, respectively (Elkayam et al., 2012), PDB 4F3T. Selected residues and moieties are labeled in colors matching those used for the protein and RNA molecules that constitute the respective complexes. Illustration generated with the program UCSF Chimera (Pettersen et al., 2004).

lacks R812 that interacts with the 5′-phosphate directly and via water (P1) and R792 that interacts with P3 in the Ago2 complex; both are part of the PIWI domain.

An interesting observation concerns the ribose conformation of UMP in the MID complex and pU (AS1) at the 5′-end of the guide strand in complex with full-length Ago2 (Fig. 5). Thus, the pucker of these residues is in the C2′-*endo* or South range of the pseudorotation phase cycle. A closer examination of more structures reveals that this is a recurring feature of Ago2 complexes, and that the 5′-terminal nucleotide adopts either a C2′-*endo* or the neighboring C1′-*exo* pucker (Egli & Manoharan, 2019). The metabolic stability of the guide strand and stable phosphorylation of its 5′-terminus are critical for siRNA activity. RNA, DNA, 2′-OMe-RNA, and 2′-F RNA are all tolerated at the AS1 position and the (*E*)-vinylphosphonate moiety precludes dephosphorylation and rephosphorylation of the guide strand (Elkayam et al., 2017). Alternative modifications at the 5′-end of the guide strand continue to be evaluated.

In the recently published crystal structures of MID in complex with either 8-Br-AMP or 6-mCEPh-purine (Shinohara et al., 2021), the conformations of the ribose do not match those in the complexes with UMP and AMP or the puckers of AS1 in the structures of miRNA or siRNAs with full-length Ago2, i.e., C2′-*endo* or C1′-*exo* (Elkayam et al., 2012; Elkayam et al., 2017; Frank et al., 2010; Schirle & MacRae, 2012). The pucker of the ribose in 8-Br-AMP is C4′-*exo*, possibly due to the bromine at the C8 position. The pucker of the ribose in 6-mCEPh-purine is C3′-*endo* and possibly the result of additional interactions of the modified base with residues of the abovementioned P523 to P527 loop (Fig. 4).

To potentially determine structures of new 5′-guide strand modifications as well as di- and trinucleotides bound to MID, we developed an alternative approach for growing crystals of complexes that precludes removal of the MID fusion partner (His_6-SUMO) prior to crystallization by relying on in situ proteolysis. Also, our procedure skips the soaking step of MID-phosphate crystals by equilibrating an all-in-one crystallization drop containing His_6-SUMO-MID, Ulp1 protease, nucleotide, buffer, and precipitant against the well solution (Basic Protocol 1). In addition, we present a fluorescence-based assay to measure the dissociation constant K_d of MID-nucleotide complexes (Basic Protocol 2).

BASIC PROTOCOL 1

CRYSTALLIZATION OF AGO2 MID-NUCLEOTIDE COMPLEXES

This protocol describes the crystallization of Ago2 MID domain complexes with nucleotides from a mixture of His_6-SUMO-MID fusion protein, Ulp1 protease, nucleotide and crystallization buffer and precipitant. DNA encoding residues 439-578 of hAgo2 MID was cloned into the pSMT3 vector (Mossessova & Lima, 2000) at the BamHI and NotI sites; the vector contains an N-terminal, Ulp1 cleavable His_6-SUMO fusion (Frank, 2011; Frank et al., 2010). The plasmid was a gift from Prof. Bhushan Nagar (McGill University, Montreal, Quebec, Canada). His_6-SUMO-MID fusion protein was expressed in BL21(DE)3 cells, and purified by Ni-affinity chromatography, ion-exchange chromatography (Q and S columns), and Superdex-75 size exclusion chromatography. Briefly, after expression suspended cells were lysed and sonicated with Buffer A consisting of 50 mM Tris·HCl pH 7.8, 20% glycerol, 800 mM NaCl, 3 mM beta-mercaptoethanol (BME), 0.5 mM tris(2-carboxyethyl)phosphine (TCEP), and 10 mM imidazole. Following centrifugation, cat. no. 355884, the supernatant was loaded onto the Ni column, washed with Buffer A, and then eluted with 400 mM imidazole. After diluting NaCl to a 50 to 80 mM concentration, the sample was passed over a Q column and then loaded onto an S column. Using a gradient of Buffer B [50 mM Tris·HCl pH 7.8, 1 mM dithiothreitol (DTT) and up to 1M NaCl], the protein was eluted when NaCl reached a concentration of 400 mM. Finally, the sample was run on a Superdex-75 size exclusion column with Buffer C consisting of 25 mM Tris·HCl pH 8.0, 150 mM NaCl, and 3 mM DTT. The purified His_6-SUMO-MID protein was concentrated to 15 mg/ml. The protein was >95% pure based on SDS-PAGE. The identity of the MID domain fusion protein was established by tryptic digestion in combination with MS analysis.

Materials

15 mg/ml His_6-SUMO-MID protein (see above)
UMP (Sigma, CAS no. 3387-36-8)
UTP (Millipore Sigma, CAS no. 19817-92-6)
tTTP (2′-3′ linked α-L-threofuranosyl thymidine-3′-triphosphate) (Zhang et al., 2013)
H_2O, nuclease free (Promega, cat. no. P119E-C)
Ulp1 protease (His-tagged SUMO protease, Vanderbilt Center for Structural Biology *https://structbio.vanderbilt.edu/wetlab/private/vectors/Ulp1/Purif.Ulp1.pdf*; or ThermoFisher Scientific, cat. no. 12588018)
Index screen, 96-condition crystallization kit (Hampton Research, cat. no. HR2-144)
Paratone-N oil, Parabar 10312 (Hampton Research, cat. no. HR2-643)

Columns for His_6-SUMO-MID protein purification (see above):
  Q sepharose fast flow (GE Healthcare, cat. no. 17-0510-01)
  SP sepharose fast flow (GE Healthcare, cat. no. 17-0720-01)
  Superdex 75 10/30 GL (GE Healthcare, cat. no. 17-5174-01)
1.5-ml Eppendorf tubes
Ice
MRC 2 crystallization plates (Hampton Research, cat. no. HR3-082)
Microscope
75-μm MicroMount (MiTeGen, cat. no. M2-)
Liquid N_2
Crystal imager (Formulatrix imager with UV fluorescence detector)

1. In an Eppendorf tube mix His_6-SUMO-MID protein with nucleotide ligand, e.g., UMP, UTP, tTTP (in nuclease-free water), in a 1:700 to 1:1000 molar ratio and store the tube on ice for 2 hr.

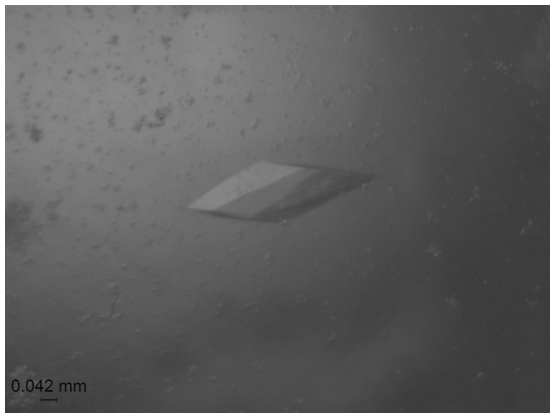

Figure 6 Crystal of Ago2 MID-UMP complex grown with Hampton Index screen condition 20.

2. Add Ulp1 protease in a 1:1000 (w/w) ratio of Ulp1:His_6-SUMO-MID.
3. Using the Index crystallization screen, set up sitting drops in a 96-well MRC 2 crystallization plate by mixing 200 nl of the His_6-SUMO-MID/nucleotide/Ulp1 solution from step 2 with 200 nl of the individual screen condition. Equilibrate each drop against 80 μl of the particular screen solution.
4. Check the plate once every 24 hr using a microscope; crystals typically appeared after 3 to 7 days (Fig. 6) with Index screen conditions 20 (0.1 M HEPES pH 7.5, 1.4 M sodium citrate tribasic dihydrate), 21 (1.8 M ammonium citrate tribasic pH 7.0), and 23 (2.1 M DL-malic acid pH 7.0).
5. Mount crystal in a 75-μm MiTeGen MicroMount following cryo-protection with Paratone-N taking care to remove excess oil before plunging in liquid nitrogen. Store in liquid nitrogen prior to X-ray diffraction data collection (Table 1).

X-ray diffraction data collection

6. Diffraction data were collected using the D8 Venture (Bruker AXS, Madison, WI) system in the Biomolecular Crystallography Facility at the Vanderbilt University Center for Structural Biology. The system includes an Excillum D2+ MetalJet X-ray source operated at 250W with Helios MX optics providing Ga Kα radiation at 1.3418 Å wavelength. The crystal was mounted on a kappa axis goniometer and maintained at 100K using an Oxford Cryosystems Cryostream 800 cryostat. The detector was a PHOTON III C14 charge-integrating pixel array detector. Data collection was performed in shutterless mode. Data were reduced using Proteum3 software (Bruker AXS, Madison, WI).

Phasing and model refinement

7. Diffraction data were phased by molecular replacement using PDB code 3LUJ. All model building and refinements were done using PHENIX (Afonine et al., 2012; Liebschner et al., 2019; Williams et al., 2018). Final checking was done using PDB-REDO (Joosten et al., 2014), which included TLS refinement. Models were placed in the unit cell using ACHESYM (Kowiel et al., 2014). Manual fitting and examination of the structures was done using COOT (Casañal et al., 2020; Emsley et al., 2010).

MEASUREMENT OF DISSOCIATION CONSTANT K_D BETWEEN AGO2 MID AND NUCLEOTIDES

BASIC PROTOCOL 2

This protocol describes the determination of K_d values for complexes between hAgo2 MID and nucleoside 3′,5′-bisphosphates, i.e., uridine-3′,5′-bisphosphate,

Table 1 Crystal Data, X-ray Data Collection, and Refinement Parameters for MID-Nucleotide Complexes[a]

Parameter	MID-UMP complex	MID-UTP complex	MID-tTTP complex
Space group	*P*1	*P*1	*P*1
Complexes/unit cell	3	3	3
Unit cell constants *a*, *b*, *c* (Å); α, β, γ (°)	$a = 39.608$ $b = 46.339$ $c = 64.920$ $\alpha = 87.58$ $\beta = 74.68$ $\gamma = 85.87$	$a = 40.106$ $b = 46.511$ $c = 65.240$ $\alpha = 87.78$ $\beta = 74.53$ $\gamma = 85.41$	$a = 37.549$ $b = 46.899$ $c = 66.209$ $\alpha = 86.74$ $\beta = 74.02$ $\gamma = 84.76$
Data collection	In-house	In-house	In-house
X-ray instrument	Bruker MetalJet	Bruker MetalJet	Bruker MetalJet
Wavelength (Å)	1.342	1.342	1.342
Resolution (Å)	21.58-1.595 (1.652-1.595)	20.53-1.78 (1.844-1.78)	20.5-1.90 (1.93-1.90)
Total reflections	856,515 (59,080)	337,798 (25,492)	186,059 (4801)
Unique reflections	118,253 (11,241)	86,315 (8459)	41,796 (1612)
Multiplicity	7.2 (5.0)	3.9 (3.0)	4.5 (3.0)
Completeness (%)	99.17 (94.79)	98.88 (97.57)	99.04 (99.21)
Mean I/σ (I)	15.20 (1.98)	5.72 (0.68)	7.48 (0.11)
R-merge	0.082 (0.835)	0.120 (2.263)	0.061 (7.834)
R-meas	0.088 (0.937)	0.138 (2.729)	0.068 (9.535)
R-pim	0.031 (0.418)	0.066 (1.501)	0.029 (5.354)
CC1/2	0.999 (0.587)	0.994 (0.273)	0.999 (0.247)
CC	1 (0.86)	0.999 (0.655)	1 (0.629)
Refl. used in ref.	117,364 (11,235)	85,817 (8448)	33,833 (1385)
Refl. used for R-free	5,665 (509)	4221 (429)	1710 (49)
R-work	0.1645 (0.2667)	0.1902 (0.3733)	0.2504 (0.4082)
R-free	0.1892 (0.2885)	0.2346 (0.4262)	0.2885 (0.4300)
CC (work)	0.972 (0.824)	0.970 (0.589)	–
CC (free)	0.959 (0.758)	0.961 (0.579)	–
No. non-H atoms	3607	3530	3268
No. macromol. atoms	3132	3084	3118
No. ligand atoms	0	87	84
No. of solvent mols.	475	359	68
Protein residues	394	396	400
R.m.s.d. bonds (Å)	0.011	0.009	0.023
R.m.s.d. angles (°)	0.95	0.88	1.74
Ramachandran favored (%)	99.74	99.74	99.49
Ramachandran allowed (%)	0.26	0.26	0.25
Ramachandran outliers (%)	0.00	0.00	0.25
Rotamer outliers (%)	0.00	0.29	2.89
Clashscore	3.77	4.06	8.22

(*Continued*)

Table 1 Crystal Data, X-ray Data Collection, and Refinement Parameters for MID-Nucleotide Complexes[a], *continued*

Parameter	MID-UMP complex	MID-UTP complex	MID-tTTP complex
Avg. B (Å^2)	19.0	28.2	36.9
Avg. B macrom. (Å^2)	17.5	26.6	34.5
Avg. B ligand (Å^2)	–	56.1	112.9
Avg. B solvent (Å^2)	29.13	35.24	49.5
No. of TLS grps.	0	3	3
PDB ID code	9BF2	9BF0	9BEZ

[a] Numbers in parentheses refer to the outermost shell.

2′-*O*-methyl-uridine-3′,5′-bisphosphate, and 2′-*O*-methyl-uridine-3′-phosphate, 5′-(*E*)-vinylphosphonate, that carry a 3′-terminal 1-(5-azidopentyl)-3-(fluorescein-5-yl)thiourea moiety (abbreviated here as PU-Fl, Pu-Fl and VPu-Fl, respectively, Fig. 7), and 2′/3′-(N-methyl-anthraniloyl)-adenosine-5′-monophosphate (Mant-AMP, Fig. 8). As described above, the Ago2 MID domain was expressed as a fusion protein with an N-terminal

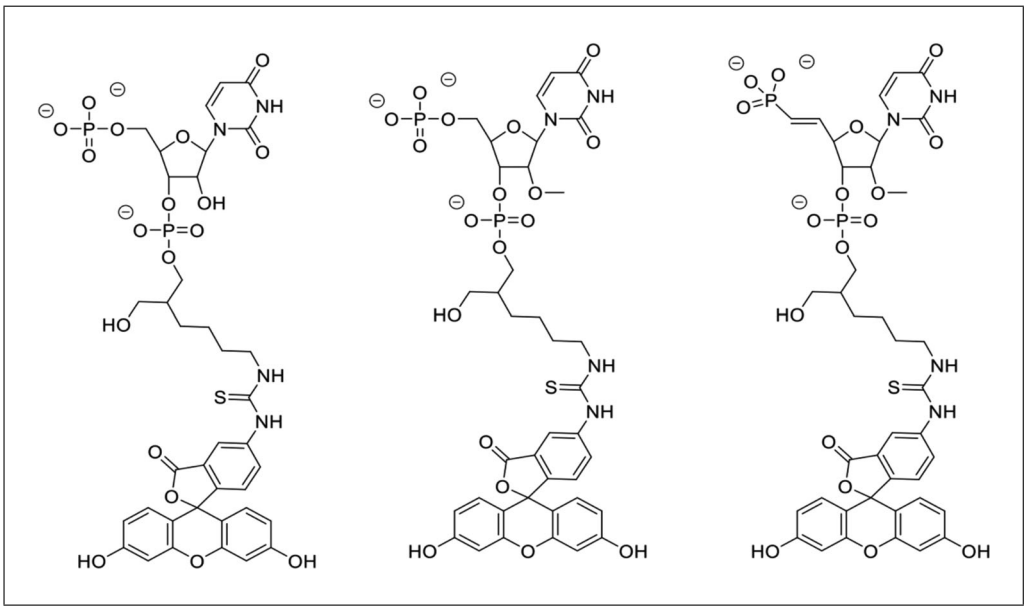

Figure 7 PU-Fl, Pu-Fl, and VPu-Fl (from left to right).

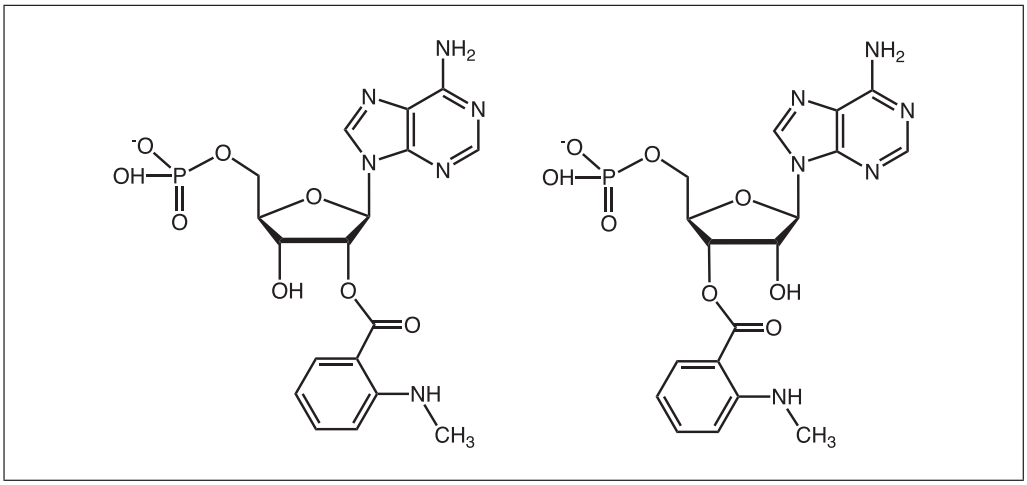

Figure 8 2′/3′-(N-methyl-anthraniloyl)-adenosine-5′-monophosphate (Mant-AMP).

cleavable His_6-SUMO tag and purified by Nickel affinity chromatography. The tag was cleaved off with Ulp1 protease and MID further purified using ion-exchange chromatography (Q and S columns), and Superdex-75 size exclusion chromatography.

Nucleoside 3′,5′-bisphosphates were prepared on a K&A oligonucleotide synthesizer using commercially available (RNA-U, 2′-OMe-U) or in-house prepared (VPu) phosphoramidites. Coupling of each phosphoramidite was performed on a commercial fluorescein support (Glen Research) using standard protocols for 2-cyanoethyl phosphoramidites. After synthesis, cleavage from the support and deprotection of any protecting groups was accomplished with either aqueous methylamine (40% aq., PU-Fl) for 90 min at 45°C or concentrated aqueous ammonium hydroxide with 5% diethylamine (Pu-Fl and VPu-Fl) for 24 hr at 30°C. Subsequent removal of the 2′-*O*-silyl protecting group in PU-Fl was accomplished using triethylamine trihydrofluoride for 90 min at 40°C. Crude bisphosphates were purified using strong anion exchange over a TSKGel SuperQ-5PW column and a linear gradient of aq. triethylammonium bicarbonate buffer (pH = 8.5, buffer B) in water (buffer A). Appropriate fractions were pooled, lyophilized to dryness, and identities of the desired products confirmed via LC-MS. The purities of the three compounds as per ion exchange (IEX) chromatography and ion pair reversed-phase (IP-RP) chromatography (IEX %/IP-RP %) were 93/96 (PU-Fl), 94/95 (Pu-Fl), and 94/99 (VPu-Fl).

We employed steady-state techniques to monitor changes in the emission intensity of fluorescein (λ_{ex} 493 nm, λ_{em} 517 nm) and Mant (λ_{ex} 355 nm, λ_{em} 448 nm). Increasing amounts of nucleotide were added to a 1 μM solution of MID and changes in fluorescence emission intensity monitored with a Fluorolog ISA Jobin Yvon-Spex spectrometer. The temperature of the cell compartment was kept at 20°C with a refrigerated circulating water bath. Measurements were corrected for dilution and blank solutions. The fluorescence emission data served as input for GraphPad Prism (version 5.00 for Mac; Graph-Pad Software, La Jolla, CA; *https://www.graphpad.com/*). We selected a nonlinear regression (curve fit) in combination with the equation for "one site-specific binding" to compute K_d values for MID-nucleotide complexes.

Materials

1 μM Ago2 MID domain (see above)
PU-Fl, Pu-Fl, and VPu-Fl nucleotides (Alnylam Pharmaceuticals, synthesized)
H_2O, nuclease free (Promega, cat. no. P119E-C)
Mant-AMP (Jena Bioscience, cat. no. NU-236S)
Binding buffer (10 mM HEPES pH 7.4, 150 mM NaCl, 3 mM EDTA, 5mM TCEP) (Current Protocols, 2006)

1-ml cuvette
Micropipette
Fluorometer (Fluorolog ISA Jobin Yvon-Spex spectrometer)
Computer with analysis software (e.g., GraphPad Prism)

1. In a cuvette that contains 1 ml of a 1 μM solution of MID protein, by adding 1 μl of a nucleotide solution (in nuclease-free water) in a stepwise fashion, increase the concentration of the latter from 0 to 100 nM, 200 nM, 300 nM, 400 nM, 600 nM, 800 nM, 1 μM, 2 μM, 3 μM, 4 μM.
2. Prior to and after adding nucleotide solution, measure the fluorescence emission intensity at 517 nm (fluorescein-labeled nucleotides PU-Fl, Pu-Fl, and VPu-Fl) or 448 nm (Mant-AMP).
3. Apply corrections for blank (buffer only) solution and dilution to the emission intensity data.

4. Use individual wavelength-emission intensity pairs as input for Graph-Pad and compute a curve fit using the nonlinear regression option in combination with the equation for "one site-specific binding" to extract the K_d value.

COMMENTARY

Background Information

Oligonucleotide therapeutics currently approved for diverse indications (Egli & Manoharan, 2023) and candidates in clinical trials at various stages (Crooke et al., 2018; Moumné et al., 2022; Shen & Corey, 2018) all feature extensive chemical modification. Modifications afford metabolic stability, facilitate cellular uptake, allow targeting of specific organs and tissues, and can mediate favorable interactions with proteins and enzymes. Five of the six siRNA therapeutics approved by the FDA since 2018, GIVLAARI, OXLUMO, LEQVIO, AMVUTTRA (Egli & Manoharan, 2023), and RIVFLOZA (Liu et al., 2022; Syed, 2023; *https://www.accessdata.fda.gov/drugsatfda_docs/label/2023/215842s000lbl.pdf*) are composed of fully 2′-fluoro/2′-*O*-methyl-modified RNA guide (antisense, AS) and passenger (sense, S) strands. The passenger strands of these siRNAs also feature GalNAc conjugates for efficient delivery to hepatocytes that is mediated by asialoglycoprotein receptor (ASGPR) (Egli & Manoharan, 2023; Kandasamy et al., 2023). In addition, phosphate groups at the 5′-ends of both guide and passenger strand and the 3′-end of the guide strand are replaced by phosphorothioates for enhanced protection against exonuclease attack (Eckstein, 1985; Egli & Manoharan, 2023; Hyjek-Skladanowska et al., 2020; Jahns et al., 2022).

siRNA strands are comprised of between 21 and 23 nucleotides. The varying nature of interactions with the Ago2 endonuclease of the RNA-induced silencing complex (RISC) along the guide and passenger siRNAs presents abundant opportunities for regiospecific chemical modification (Egli & Manoharan, 2019). Thus, modifying the 5′-terminal ends of siRNAs can enhance the discrimination between the guide and passenger strands to reduce off-target effects (Datta et al., 2023; Kumar et al., 2019). The favorable properties of the 2′-fluoro and 2′-*O*-methyl ribonucleotide analogs as modifiers of siRNAs were recognized early on (Manoharan et al., 2011). The 2′-fluoro modification is tolerated at all positions but does not alone afford sufficient protection against nuclease degradation. 2′-*O*-methyl ribonucleotides are more protective by comparison and are sterically tolerated at most locations in the two strands. The second nucleotide of the guide strand (AS2) constitutes a notable exception in this regard as modification there is limited to either 2′-deoxy or 2′-fluoro residues (Egli & Manoharan, 2019). A sharp turn in the seed region (AS2 to AS8) between nucleotides 6 and 7 seen in crystal structures of Ago2 complexes (Elkayam et al., 2012; Schirle & MacRae, 2012) led us to deploy modifications that destabilize seed pairing and preorganize the guide strand for this wrinkle, resulting in improvements in loading, mitigation of off-target effects, and better clinical safety (Egli et al., 2023; Guenther et al., 2022; Matsuda et al., 2023; Schlegel et al., 2022). Lipophilic modification in the form of a 2′-*O*-hexadecyl conjugation at position 16 of the sense strand was shown to result in potent and durable silencing in the central nervous system (CNS) (Brown et al., 2022).

Unlike the siRNA passenger strand, the siRNA guide strand carries a 5′-phosphate group. This phosphate group is captured by the Ago2 MID domain (Figs. 1 and 4), locks the guide strand into position during the loading process and makes a key contribution to the discrimination between the guide and passenger siRNAs. However, the 5′-phosphate group is not metabolically stable and can be removed, thereby affecting loading efficiency and the stability of the RISC complex. Replacing the phosphate with an (*E*)-vinylphosphonate (VP) moiety protects the 5′-end of the guide (Elkayam et al., 2017). The VP modification is an excellent electrostatic and steric mimic of the native phosphate, the latter thanks to the antiperiplanar conformation of the β torsion angle of the AS1 nucleotide in crystal structures (Fig. 4) (Egli & Manoharan, 2019). The VP modification is not yet a feature of currently approved siRNA therapeutics (Egli & Manoharan, 2023); RIVFLOZA contains a methylenephosphonate moiety at the 5′-terminus of the guide strand (Liu et al., 2022; Syed, 2023). Another noteworthy distinction of the AS1 nucleotide is its C2′-*endo* or C1′-*exo* B form–like sugar pucker (Figs. 4 and 5) (Egli & Manoharan, 2019). In addition to the negative charge, this conformational constraint is an important point to consider when designing

modifications to replace the AS1 nucleotide. Besides molecular modeling, experimental structure determination is an important tool in the design of new siRNA modifications and is required to visualize the conformational properties of new analogs and their interactions with MID and other Ago2 domains (Egli & Manoharan, 2019). For example, the crystal structure of 6-mCEPh-purine bound to MID exhibits a North C3′-*endo* pucker (Shinohara et al., 2021) and therefore does not mimic the sugar conformation of the parent AS1 ribonucleotides (Figs. 4 and 5).

Crystals of MID complexes with NMPs are obtained by soaking crystals of the domain with phosphate trapped at the binding site in solutions of the nucleotide to displace phosphate (Frank, 2011; Frank et al., 2010). Such crystals are of space group *P*1 with three molecules per asymmetric unit (Frank et al., 2010). Concentrating the MID protein following removal of the His_6-SUMO tag to levels typically used for crystallization, i.e., several mg/ml, particularly under low salt conditions, is hampered by MID frequently precipitating. To circumvent this issue, we explored the use of the MID fusion protein without removal of the tag for crystallization of nucleotide complexes in the presence of Ulp1 protease in a single step (Basic Protocol 1). As an alternative to the published protocol that used solution NMR (Frank et al., 2010), we relied on fluorescence spectrometry in combination with suitably modified nucleotides to measure dissociation constants of MID-nucleotide complexes (Basic Protocol 2).

Critical Parameters and Troubleshooting

The solubility of the His_6-SUMO-MID protein is much higher than that of the MID domain alone and solutions of the fusion protein can be concentrated to 15 mg/ml without risking precipitation under relatively low salt conditions and stored at −80°C for several months. Instead of removing the His_6-SUMO tag in a separate step and purifying the MID domain chromatographically, our protocol directly uses the purified fusion protein for crystallization setups. In situ proteolysis to free the MID domain in the presence of nucleotide and crystallization buffer and precipitant requires optimization of the relative concentrations of MID, Ulp1 protease and nucleotide. A 1000:1 ratio of His_6-SUMO-MID:Ulp1 produced the best crystals.

In a previously developed protocol to crystallize membrane-bound cytochrome P450 enzymes in the presence of protease to shorten the N-terminal tail that had been modified with a leader sequence of reduced hydrophobicity to boost expression, we tested 12 different proteases and found that trypsin and subtilisin produced viable crystals of N-terminally truncated enzymes (Lei & Egli, 2016). The ratios of P450:protease tested ranged between 100:1 to 2000:1 and optimal crystals of zebrafish P450 17A1 (with subtilisin) and P450 17A2 (with trypsin) were obtained using a P450:protease ratio of 1000:1.

Unlike the Ulp1 protease that is used in much lower concentrations than the His_6-SUMO-MID fusion protein (consistent with the catalytic activity of the former), the nucleotide needs to be present in the crystallization drop at much higher concentrations than the MID fusion protein. Diffraction-quality crystals were obtained with a nucleotide:His_6-SUMO-MID molar ratio of between 700:1 to 1000:1. Because the stock solution of the fusion protein is ∼1 mM, the nucleotide concentration needs to reach 1 M or higher. This can pose problems with nucleotides that are not as soluble as UMP or UTP, e.g., 5′-pUpU-3′ dimers or 5′-pUpUpU-3′ trimers. An excess of nucleotide will ensure that MID protein without the His_6-SUMO tag encounters enough ligand molecules to drive crystal formation of complex rather than causing MID to precipitate. Unlike with soaks of MID-phosphate crystals in solutions of the nucleotide ligand (Frank et al., 2010), the all-in-one drop crystallization protocol described here and using His_6-SUMO-MID fusion protein may not require displacement of intrinsically bound phosphate from MID to produce crystals of the MID-nucleotide complex. However, we cannot rule out that His_6-SUMO-MID protein contains some bound phosphate following expression and purification.

The need for very high concentrations of the nucleotide ligand may limit the chances to grow crystals of dimers and trimers bound to MID using our approach. The presence of at least one 5′-terminal phosphate group (NMP) in the ligand is another requirement for successful crystallization of MID complex. For example, we could not grow crystals of MID with uridine (U) or 5′-UpUpU. Clearly, the phosphodiester groups of 5′-UpUpU cannot serve as substitutes for a terminal phosphate, unlike the first phosphodiester (bold font) in m^7G**p**ppG (Fig. 3). However, in the latter compound that phosphate is accompanied by two more phosphates that glue together the complex. The crystal structure of the

complex with m^7GpppG may raise hopes that MID can be crystallized with di- and trinucleotides, such as 5′-pUpU and 5′-pUpUpU, respectively. In other words, because **G** of m^7Gppp**G** is ordered in the electron density despite the absence of interactions with MID residues or those from neighboring MID domains or dinucleotides in the crystal lattice (Fig. 3; Frank et al., 2011), it might be possible to visualize U2 or U2 and U3 in structures of complexes with 5′-pUpU or 5′-pUpUpU, respectively. However, we could not produce viable crystals of such complexes. This may in part be due to limitations with reaching high enough concentrations of dimers and trimers as alluded to above. Also, the orientation of the **ppG** moiety in the structure of the complex with m^7Gp**ppG** (Fig. 3) extends in the opposite direction and away from the locations of AS2 and AS3 in the complex of guide siRNA with Ago2 (Fig. 5). Similarly, we could not grow crystals of MID with 5′-pUp using our protocol and attempts to obtain crystals of a complex with Mant-AMP (Fig. 8) also failed.

Interestingly, the dissociation constants between MID and ligands that feature both 5′- and 3′-phosphate groups, such as PU-Fl, Pu-Fl, and VPu-Fl (Fig. 7), indicate tighter binding compared to the complex between MID and Mant-AMP (see Understanding Results). This suggests that the 3′-phosphate may contribute to binding, perhaps by interacting with Q548, K550, and N551 as seen in the structure of Ago2 bound to miR-20a (Fig. 5). For now, it seems that crystal structures of complexes of the Ago2 MID domain alone can only be obtained with mononucleotides and select compounds like m^7GpppG. MID complexes with longer pieces of RNA have all resisted crystallization, which we rationalize with the inability of the domain alone to sufficiently constrain the second and third nucleotide.

Understanding Results

We crystallized complexes of human Ago2 MID with UMP, UTP, and tTTP and determined their structures at resolutions of up to 1.59 Å (Table 1). The structures with UMP and UTP closely resemble those previously reported for the same monophosphate (Fig. 4A) (Frank et al., 2010) and ATP (Fig. 2A and B) (Frank et al., 2011), respectively. The space group in all cases is *P*1 as reported for other MID complexes. Our Basic Protocol 1 using in situ proteolysis of the His_6-SUMO-MID fusion protein to grow crystals of MID-nucleotide complexes does not affect crystal form and packing. Using pure fusion protein in combination with Ulp1 protease in the crystallization drop circumvents the need for extra purification steps following cleavage of the His_6-SUMO tag. Further advantages of our protocol are the reduced risk of purified MID precipitating at the higher concentrations needed for crystallization and having to compete with bound phosphate when soaking MID crystals in solutions of nucleotides. However, the all-in-one-drop approach requires high concentrations of the nucleotide ligand. This requirement does not pose problems with UMP, UDP, UTP, tTTP, etc., but less soluble ligands could prove more challenging in this regard. As indicated above, dimers and trimers did not produce viable crystals of MID complexes. We obtained crystals of the complex with nicotinamide adenine dinucleotide phosphate (NADPH) that exhibited a different morphology than MID-UMP complex crystals (Fig. 6). However, these crystals only diffracted to low resolution and were not suitable for structure determination.

The structure of the MID complex with tTTP reveals an orientation of the TNA triphosphate that differs from that of UMP (Fig. 9). The positions of the α-phosphate groups are separated by ∼1.3Å, whereby the UMP phosphate sits deeper inside the MID binding pocket. Their sugar conformations differ in that tTTP adopts the expected C4′-*exo* pucker whereas UMP has a C2′-*endo* pucker. In addition, the tTTP base does not stack on T529; instead, the nucleoside has shifted somewhat relative to uridine and thymine engages in a partial stacking interaction with the side chain of Q548 (Fig. 9). The latter residue usually forms a H-bond with the first bridging phosphate of the guide strand along with N551 (Fig. 5). The two MID residues contribute to stabilizing a sharp turn in the RNA strand between AS1 and AS3. The absence of the second nucleotide together with PIWI residues of Ago2 that interact with the 5′-terminal region of the guide strand expose limitations of MID complexes alone with regards to studying the conformation of that region of modified guides and interactions with Ago2. Thus, a computational model of miR-20a with a 5′-tTMP that adopts a C4′-*exo* pucker in place of UMP and bound to Ago2 demonstrates that TNA can stack on Y529 and mimic the tight turn between AS1 and AS3 in principle (Matsuda et al., 2023).

K_d values for MID-nucleotide complexes based on concentration-dependent fluorescence emission intensity measurements as described in Basic Protocol 2 are consistent with

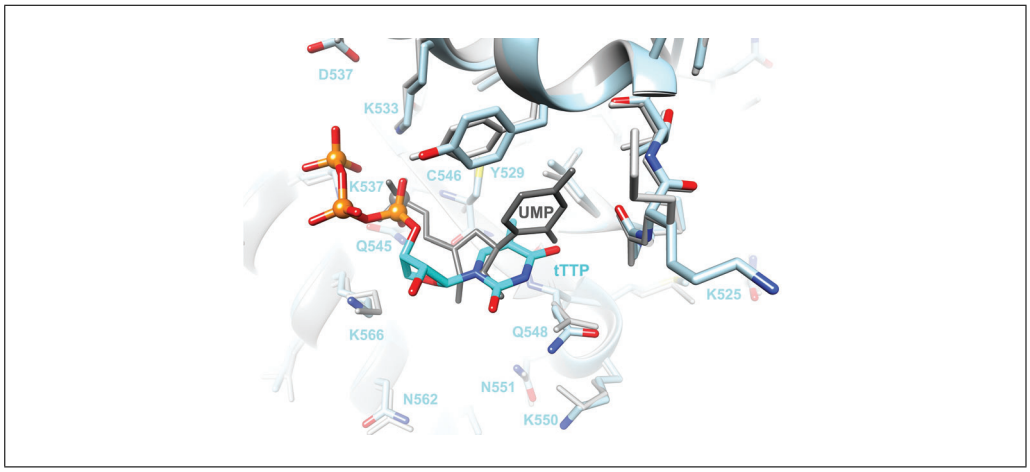

Figure 9 Overlay of the structures of MID complexes with tTTP and UMP. Nucleotide carbon atoms are colored in cyan and dark gray, respectively, and phosphorus atoms are highlighted as spheres. The protein portion of the MID-UMP complex is colored in light gray. Ribbon cartoon and side chain carbon atoms in the MID-tTTP complex are colored in light blue. Solvent molecules have been omitted for clarity. Illustration generated with the program UCSF Chimera (Pettersen et al., 2004).

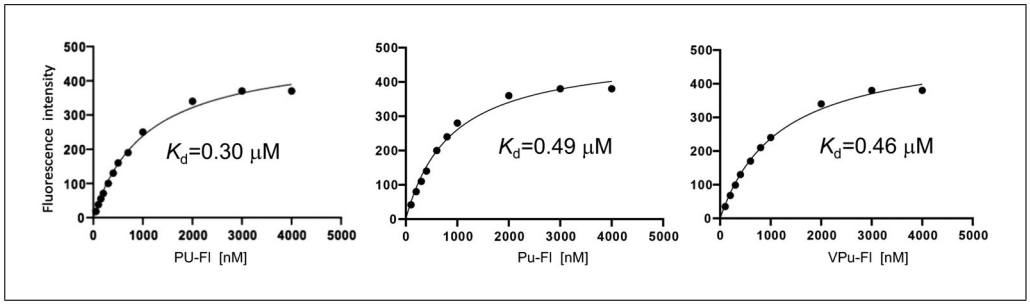

Figure 10 Stabilities of MID complexes with nucleotides PU-Fl (left), Pu-Fl (center), and VPu-Fl (right).

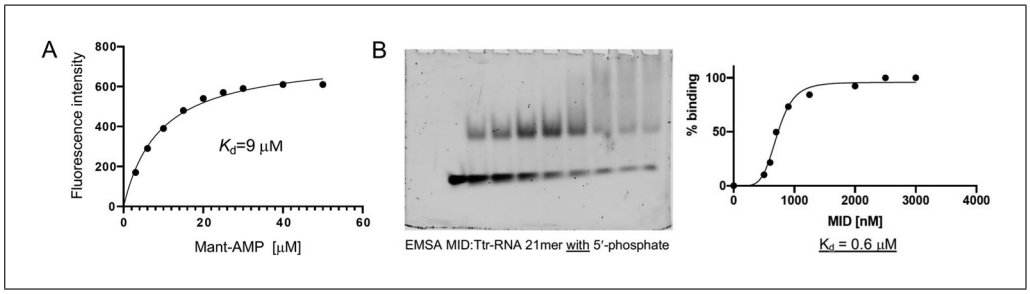

Figure 11 (**A**) Stability of the complex between MID and Mant-AMP using Basic Protocol 2. (**B**) Stability of the complex between MID and a 21-mer RNA carrying a 5′-terminal phosphate based on EMSA.

sub-μM affinities for PU-Fl, Pu-Fl, and VPu-Fl (Figs. 7 and 10). The dissociation constants of between 0.30 and 0.49 μM and using a 1 μM solution of MID indicate a significantly tighter binding than that reported for UMP based on ^{1}H-^{15}N HSQC NMR and using 0.1 to 0.25 mM MID (K_d = 120 μM; Frank et al., 2010). To examine whether this difference could at least in part be related to the presence of a 3′-phosphate in the three nucleotides we had tested, we also measured the K_d for the MID complex with Mant-AMP (Fig. 8). Indeed, in the absence of the 3′-phosphate, the stability of the complex is reduced to 9 μM (Fig. 11A). However, this K_d still indicates ca. 30-fold tighter binding of AMP compared to the previously reported stability of the MID-AMP complex using HSQC NMR: K_d = 260 μM (Frank et al., 2010). The tighter binding as seen with the bisphosphates (Fig. 10) is supported by an independent electrophoretic mobility shift assay (EMSA) for a complex

between Ago2 MID and an RNA 21-mer (Fig. 11B) using a previously published protocol (Seo et al., 2019).

Time Considerations

Expression and purification of the His_6-SUMO-MID protein can be accomplished in 2 days. The preparation and purification of the fluorescently labeled nucleotides PU-Fl, Pu-Fl, and VPu-Fl takes ∼5 days. Collecting the fluorescence emission data for a MID-nucleotide complex including solution preparation and titration requires ∼2 hr, and data transfer and computing the K_d value using Graph-Pad Prism takes 1 hr.

Acknowledgments

This work was supported by Alnylam Pharmaceuticals, Vanderbilt University, and US National Science Foundation Award MCB-2224897. We thank Dr. Filipp Frank for helpful discussions.

Author Contributions

Li Lei: Conceptualization; formal analysis; investigation; methodology; resources; writing—original draft. **Joel M. Harp**: Data curation; formal analysis; writing—original draft. **John C. Chaput**: Resources. **Kelly Wassarman**: Methodology; resources; writing—original draft. **Mark K. Schlegel**: Methodology; resources; writing—original draft. **Muthiah Manoharan**: Resources; supervision. **Martin Egli**: Conceptualization; formal analysis; methodology; resources; supervision; validation; writing—original draft; writing—review and editing.

Conflict of Interest

The authors declare no conflict of interest.

Data Availability Statement

PDB ID codes: 9BF2 (MID-UMP complex), 9BF0 (MID-UTP complex), and 9BEZ (MID-tTTP complex).

Literature Cited

Afonine, P. V., Grosse-Kunstleve, R. W., Echols, N., Headd, J. J., Moriarty, N. W., Mustyakimov, M., Terwilliger, T. C., Urzhumtsev, A., Zwart, P. H., & Adams, P. D. (2012). Towards automated crystallographic structure refinement with phenix.refine. *Acta Crystallographica. Section D, Structural Biology*, *68*, 352–367. https://doi.org/10.1107/S0907444912001308

Berman, H. M., Westbrook, J., Feng, Z., Gilliland, G., Bhat, T. N., Weissig, H., Shindyalov, I. N., & Bourne, P. E. (2000). The protein data bank. *Nucleic Acids Research*, *28*, 235–242. https://doi.org/10.1093/nar/28.1.235

Brown, K. M., Nair, J. K., Janas, M. M., Anglero-Rodriguez, Y. I., Dang, L. T. H., Peng, H., Theile, C. S., Castellanos-Rizaldos, E., Brown, C., Foster, D., Kurz, J., Allen, J., Maganti, R., Li, J., Matsuda, S., Stricos, M., Chickering, T., Jung, M., Wassarman, K., … Jadhav, V. (2022). Expanding RNAi therapeutics to extrahepatic tissues with lipophilic conjugates. *Nature Biotechnology*, *40*, 1500–1508. https://doi.org/10.1038/s41587-022-01334-x

Casañal, A., Lohkamp, B., & Emsley, P. (2020). Current developments in Coot for macromolecular model building of electron cryo-microscopy and crystallographic data. *Protein Science*, *29*, 1069–1078. https://doi.org/10.1002/pro.3791

Crooke, S. T., Witztum, J. L., Bennett, C. F., & Baker, B. F. (2018). RNA-targeted therapeutics. *Cell Metabolism*, *27*, 714–739. https://doi.org/10.1016/j.cmet.2018.03.004

Current Protocols (2006). Commonly Used Reagents. *Current Protocols in Microbiology*, *00*, A.2A.1–A.2A.15. https://doi.org/10.1002/9780471729259.mca02as00

Datta, D., Theile, C., Wassarman, K., Qin, J., Racie, T., Schmidt, K., Jiang, Y., Sigel, R., Janas, M., Egli, M., & Manoharan, M. (2023). Rational optimization of siRNA to ensure strand bias in the interaction with the RNA-induced silencing complex. *Chemical Communications (Cambridge, England)*, *59*, 6347–6350. https://doi.org/10.1039/D3CC01143G

Eckstein, F. (1985). Nucleoside phosphorothioates. *Annual Review of Biochemistry*, *54*, 367–402. https://doi.org/10.1146/annurev.bi.54.070185.002055

Egli, M., & Manoharan, M. (2019). Re-engineering RNA molecules into therapeutic agents. *Accounts of Chemical Research*, *52*, 1036–1047. https://doi.org/10.1021/acs.accounts.8b00650

Egli, M., & Manoharan, M. (2023). Chemistry, structure and function of approved oligonucleotide therapeutics. *Nucleic Acids Research*, *51*, 2529–2573. https://doi.org/10.1093/nar/gkad067

Egli, M., Schlegel, M. K., & Manoharan, M. (2023). Acyclic (*S*)-glycol nucleic acid (*S*-GNA) modification of siRNAs improves the safety of RNAi therapeutics while maintaining potency. *RNA*, *29*, 402–414. https://doi.org/10.1261/rna.079526.122

Elkayam, E., Kuhn, C. D., Tocilj, A., Haase, A. D., Greene, E. M., Hannon, G. J., & Joshua-Tor, L. (2012). The structure of human Argonaute-2 in complex with miR-20a. *Cell*, *150*, 100–110. https://doi.org/10.1016/j.cell.2012.05.017

Elkayam, E., Parmar, R., Brown, C. R., Willoughby, J. L. S., Theile, C. S., Manoharan, M., & Joshua-Tor, L. (2017). siRNA carrying an (*E*)-vinylphosphonate moiety at the 5′ end of the guide strand augments gene silencing by enhanced binding to human Argonaute-2. *Nucleic Acids Research*, *45*, 3528–3536. https://doi.org/10.1093/nar/gkw1171

Emsley, P., Lohkamp, B., Scott, W., & Cowtan, K. (2010). Features and development of coot. *Acta Crystallographica. Section D, Structural Biology*, *66*, 486–501. https://doi.org/10.1107/S0907444910007493

Frank, F., Sonenberg, N., & Nagar, B. (2010). Structural basis for 5'-nucleotide base-specific recognition of guide RNA by human AGO2. *Nature*, *465*, 818–822. https://doi.org/10.1038/nature09039

Frank, F. (2011). *Structural and functional characterization of Argonaute MID domain* [unpublished Ph.D. thesis]. Department of Biochemistry, McGill University, Montreal, Quebec, Canada.

Frank, F., Fabian, M. R., Stepinski, J., Jemielity, J., Darzynkiewicz, E., Sonenberg, N., & Nagar, B. (2011). Structural analysis of 5'-mRNA-cap interactions with the human AGO2 MID domain. *EMBO Reports*, *12*, 415–420. https://doi.org/10.1038/embor.2011.48

Guenther, D. C., Mori, S., Matsuda, S., Gilbert, J. A., Willoughby, J. L. S., Hyde, S., Bisbe, A., Jiang, Y., Agarwal, S., Madaoui, M., Janas, M. M., Charisse, K., Maier, M. A., Egli, M., & Manoharan, M. (2022). Role of a "magic" methyl: 2'-deoxy-2'-α-F-2'-β-*C*-methyl pyrimidine nucleotides modulate RNA interference activity through synergy with 5'-phosphate mimics and mitigation of off-target effects. *Journal of the American Chemical Society*, *144*, 14517–14534. https://doi.org/10.1021/jacs.2c01679

Hyjek-Skladanowska, M., Vickers, T. A., Napiorkowska, A., Anderson, B. A., Tanowitz, M., Crooke, S. T., Liang, X.-H., Seth, P. P., & Nowotny, M. (2020). Origins of the increased affinity of phosphorothioate-modified therapeutic nucleic acids for proteins. *Journal of the American Chemical Society*, *142*, 7456–7468. https://doi.org/10.1021/jacs.9b13524

Jahns, H., Taneja, N., Willoughby, J. L. S., Akabane-Nakata, M., Brown, C. R., Nguyen, T., Bisbe, A., Matsuda, S., Hettinger, M., Manoharan, R. M., Rajeev, K. G., Maier, M. A., Zlatev, I., Charisse, K., Egli, M., & Manoharan, M. (2022). Chirality matters: Stereo-defined phosphorothioate linkages at the termini of small interfering RNAs improve pharmacology in vivo. *Nucleic Acids Research*, *50*, 1221–1240. https://doi.org/10.1093/nar/gkab544

Joosten, R. P., Long, F., Murshudov, G. N., & Perrakis, A. (2014). The PDB_REDO server for macromolecular structure model optimization. *IUCrJ*, *1*, 213–220. https://doi.org/10.1107/S2052252514009324

Kandasamy, P., Mori, S., Matsuda, S., Erande, N., Datta, D., Willoughby, J. L. S., Taneja, N., O'Shea, J., Bisbe, A., Manoharan, R. M., Yucius, K., Nguyen, T., Indrakanti, R., Gupta, S., Gilbert, J. A., Racie, T., Chan, A., Liu, J., Hutabarat, R., … Manoharan, M. (2023). Metabolically stable anomeric linkages containing GalNAc-siRNA conjugates: An interplay among ASGPR, glycosidase, and RISC pathways. *Journal of Medicinal Chemistry*, *66*, 2506–2523. https://doi.org/10.1021/acs.jmedchem.2c01337

Kowiel, M., Jaskolski, M., & Dauter, Z. (2014). ACHESYM: An algorithm and server for standardized placement of macromolecular models in the unit cell. *Acta Crystallographica. Section D, Structural Biology*, *70*, 3290–3298. https://doi.org/10.1107/S1399004714024572

Kumar, P., Parmar, R. G., Brown, C. R., Willoughby, J. L. S., Foster, D. J., Babu, I. R., Schofield, S., Jadhav, V., Charisse, K., Nair, J. K., Rajeev, K. G., Maier, M. A., Egli, M., & Manoharan, M. (2019). 5'-Morpholino modification of the sense strand of an siRNA makes it a more effective passenger. *Chemical Communications (Cambridge, England)*, *55*, 5139–5142. https://doi.org/10.1039/C9CC00977A

Lei, L., & Egli, M. (2016). In situ proteolysis for crystallization of membrane bound cytochrome P450 17A1 and 17A2 proteins from zebrafish. *Current Protocols in Protein Science*, *84*, 29.16.1–29.16.19. https://doi.org/10.1002/0471140864.ps2916s84

Liebschner, D., Afonine, P. V., Baker, M. L., Bunkóczi, G., Chen, V. B., Croll, T. I., Hintze, B., Hung, L. W., Jain, S., McCoy, A. J., Moriarty, N. W., Oeffner, R. D., Poon, B. K., Prisant, M. G., Read, R. J., Richardson, J. S., Richardson, D. C., Sammito, M. D., Sobolev, O. V., … Adams, P. D. (2019). Macromolecular structure determination using X-rays, neutrons and electrons: Recent developments in Phenix. *Acta Crystallographica. Section D, Structural Biology*, *75*, 861–877. https://doi.org/10.1107/S2059798319011471

Liu, A., Zhao, J., Shah, M., Migliorati, J. M., Tawfik, S. M., Bahal, R., Rasmussen, T. P., Manautou, J. E., & Zhong, X. B. (2022). Nedosiran, a candidate siRNA drug for the treatment of primary hyperoxaluria: Design, development, and clinical studies. *ACS Pharmacology & Translational Science*, *5*, 1007–1016. https://doi.org/10.1021/acsptsci.2c00110

Manoharan, M., Akinc, A., Pandey, R. K., Qin, J., Hadwiger, P., John, M., Mills, K., Charisse, K., Maier, M. A., Nechev, L., Greene, E. M., Pallan, P. S., Rozners, E., Rajeev, K. G., & Egli, M. (2011). Unique gene-silencing and structural properties of 2'-fluoro-modified siRNAs. *Angewandte Chemie (International ed. in English)*, *50*, 2284–2288. https://doi.org/10.1002/anie.201006519

Matsuda, S., Bala, S., Liao, J. Y., Datta, D., Mikami, A., Woods, L., Harp, J. M., Gilbert, J. A., Bisbe, A., Manoharan, R. M., Kim, M., Theile, C. S., Guenther, D. C., Jiang, Y., Agarwal, S., Maganti, R., Schlegel, M. K., Zlatev, I., Charisse, K., … Manoharan, M. (2023). Shorter Is better: The α-(L)-threofuranosyl nucleic acid modification improves stability, potency, safety, and Ago2 binding and mitigates off-target effects of small interfering RNAs. *Journal of the American Chemical Society*, *145*, 19691–19706. https://doi.org/10.1021/jacs.3c04744

Mossessova, E., & Lima, C. D. (2000). Ulp1-SUMO crystal structure and genetic analysis

reveal conserved interactions and a regulatory element essential for cell growth in yeast. *Molecular Cell*, *5*, 865–876. https://doi.org/10.1016/S1097-2765(00)80326-3

Moumné, L., Marie, A. C., & Crouvezier, N. (2022). Oligonucleotide therapeutics: From discovery and development to patentability. *Pharmaceutics*, *14*, 260. https://doi.org/10.3390/pharmaceutics14020260

Pettersen, E. F., Goddard, T. D., Huang, C. C., Couch, G. S., Greenblatt, D. M., Meng, E. C., & Ferrin, T. E. (2004). UCSF Chimera - a visualization system for exploratory research and analysis. *Journal of Computational Chemistry*, *25*, 1605–1612. https://doi.org/10.1002/jcc.20084

Schirle, N. T., & MacRae, I. J. (2012). The crystal structure of human Argonaute2. *Science*, *336*, 1037–1040. https://doi.org/10.1126/science.1221551

Schlegel, M. K., Janas, M. M., Jiang, Y., Barry, J. D., Davis, W., Agarwal, S., Berman, D., Brown, C. R., Castoreno, A., LeBlanc, S., Liebow, A., Mayo, T., Milstein, S., Nguyen, T., Shulga-Morskaya, S., Hyde, S., Schofield, S., Szeto, J., Woods, L. B., … Maier, M. A. (2022). From bench to bedside: Improving the clinical safety of GalNAc-siRNA conjugates using seed-pairing destabilization. *Nucleic Acids Research*, *50*, 6656–6670. https://doi.org/10.1093/nar/gkac539

Seo, M., Lei, L., & Egli, M. (2019). Label-free electrophoretic mobility shift assay (EMSA) for measuring dissociation constants of protein-RNA complexes. *Current Protocols in Nucleic Acid Chemistry*, *76*, e70. https://doi.org/10.1002/cpnc.70

Shen, X., & Corey, D. R. (2018). Chemistry, mechanism and clinical status of antisense oligonucleotides and duplex RNAs. *Nucleic Acids Research*, *46*, 1584–1600. https://doi.org/10.1093/nar/gkx1239

Shinohara, F., Oashi, T., Harumoto, T., Nishikawa, T., Takayama, Y., Miyagi, H., Takahashi, Y., Nakajima, T., Sawada, T., Koda, Y., Makino, A., Sato, A., Hamaguchi, K., Suzuki, M., Yamamoto, J., Tamari, Y., & Saito, J. I. (2021). siRNA potency enhancement via chemical modifications of nucleotide bases at the 5'-end of the siRNA guide strand. *RNA*, *27*, 163–173. https://doi.org/10.1261/rna.073783.119

Syed, Y. Y. (2023). Nedosiran: First approval. *Drugs*, *83*, 1729–1733. https://doi.org/10.1007/s40265-023-01976-4

Williams, C. J., Hintze, B. J., Headd, J. J., Moriarty, N. W., Chen, V. B., Jain, S., Prisant, M. G., Lewis, S. M., Videau, L. L., Keedy, D. A., Deis, L. N., Arendall, W. B. III., Verma, V., Snoeyink, J. S., Adams, P. D., Lovell, S. C., Richardson, J. S., & Richardson, D. C. (2018). MolProbity: More and better reference data for improved all-atom structure validation. *Protein Science*, *27*, 293–315. https://doi.org/10.1002/pro.3330

Zhang, S., Yu, H., & Chaput, J. C. (2013). Synthesis of threose nucleic acid (TNA) triphosphates and oligonucleotides by polymerase-mediated primer extension. *Current Protocols in Nucleic Acid Chemistry*, *52*, 4.54.1–4.54.17. https://doi.org/10.1002/0471142700.nc0454s52